Mid-infrared resonant cavity light emitting diodes operating at 4.5 µm

FURAT A. AL-SAYMARI[1,2], ADAM P. CRAIG[1], QI LU[1], ANDREW R. J. MARSHALL[1], PETER J. CARRINGTON[3] AND ANTHONY KRIER[1*]

[1]*Physics Department, Lancaster University, LA1 4YB, United Kingdom*
[2]*Department of Physics, College of Education for Pure Science, University of Basra, Basra, Iraq*
[3]*Engineering Department, Lancaster University, LA1 4YW, United Kingdom*
[*] *a.krier@lancaster.ac.uk*

Abstract: We report on a mid-infrared resonant cavity light emitting diode (RCLED) operating at the wavelength of 4.5 µm with narrow spectral linewidth at room temperature. Compared to a reference LED without a resonant cavity our RCLED exhibits (85x) higher peak intensity, (13x) higher integrated output power, (16x) narrower spectral linewidth and (7x) superior temperature stability. The device consists of a one-wavelength thick micro-cavity containing an $Al_{0.12}In_{0.88}As/InAs_{0.85}Sb_{0.15}$ quantum well active region sandwiched between two high contrast $AlAs_{0.08}Sb_{0.92}$/GaSb distributed Bragg reflector mirrors, grown lattice–matched on GaSb by molecular beam epitaxy. The high spectral brightness, narrow linewidth and superior temperature stability, are attractive features, enabling these devices to be used for detection of N_2O at 4.5 µm. We show that with only minor adjustments the gases CO_2 (4.2 µm) and CO (4.6 µm) are also readily accessible.

Keywords: Resonant cavity, LED, Mid-infrared, Bragg mirror, AlInAs/InAsSb QWs, gas detection.

1. INTRODUCTION

There is a growing requirement for light emitting diodes operating in the technologically important mid-infrared spectral range, for applications such as gas and chemical sensing, infrared scene projection, industrial process control and spectroscopy. For example, mid-infrared absorption spectroscopy is an attractive technique for monitoring greenhouse gases such as CH_4 (3.3 µm), CO_2 (4.2 µm) and N_2O (4.5 µm) because they have strong fingerprint absorptions in this spectral range, enabling gas specific detection and remote sensing. Consequently, there is an increasing demand for mid-infrared light sources and detectors at these key wavelengths. Compared with thermal sources LEDs are more robust and can be operated at high modulation rates, with low power consumption, making them better suited to portable instruments. Mid-infrared LEDs also provide a more attractive, cost-effective alternative to cascade lasers especially for widespread distributed sensing applications requiring many point sensors. A variety of prototype LEDs on InAs and GaSb substrates, have already been demonstrated for some of the target wavelengths [1-6]. There has also been significant interest in developing mid-infrared LEDs on less expensive GaAs substrates, using various buffer layer schemes to accommodate the large inherent lattice mismatch with respect to active regions of alloys and heterostructures having suitable band gaps [7]. This resulted in devices of some complexity ranging from LEDs with bulk active regions in small arrays [8-11], to multispectral mid-infrared multiple quantum well (MQW) emitters [12]. Sources with sufficiently narrow linewidth and high enough spectral intensity could also be integrated with Si/Ge waveguides [13-16]. However, due to insufficient power in the absorption band of interest (low spectral intensity), there are still relatively few examples of LED based instruments or

widespread technology uptake [17]. More recently, high emittance interband cascade LEDs (ICLEDs) have been demonstrated at $\lambda \approx 3.2$ μm [18], 3.7 μm [19] and 4.1 μm [20], but spectral linewidths are quite broad. Meanwhile, the development of emitters for 4.5 μm using InAs/Ga(As)Sb superlattices is more challenging and Joule heating becomes severe, requiring short duty cycles for characterization [21,22]. For example, a radiance of 0.5 W/cm^{2}sr at a peak wavelength of 4.6 μm has been demonstrated using a 0.1% duty cycle [23].

In this work we place the LED active region, which generates the light, at the antinode of the standing wave optical field, inside a resonant microcavity made from two distributed Bragg reflectors (DBRs), to enhance spectral intensity. Constructive interference simultaneously increases LED emission intensity and narrows the linewidth [24,25]. Such resonant cavity LEDs have been successfully developed for shorter (vis-near-infrared) wavelengths with high external quantum efficiency (~15%) [26]. There has been some research effort devoted towards resonant cavity light emitting diodes (RCLEDs) and vertical cavity surface emitting lasers (VCSELs) for mid-infrared applications [27-33]. But, there are only a limited number of reports of RCLEDs and VCSELs operating in the 4-5 μm spectral range [28,33,34]. The longest wavelength RCLEDs emit at 4.2 μm but exhibit only a low (3x) emission enhancement. As yet, there is no reported mid-IR VCSEL emission beyond 4 μm and no RCLED at 4.5 μm.

Here we present, a novel mid-infrared RCLED with narrow linewidth operating at 4.5 μm, using high refractive index contrast (Δn=0.6) $AlAs_{0.08}Sb_{0.92}$/GaSb distributed Bragg reflector (DBR) mirrors and $Al_{0.12}In_{0.88}As/InAs_{0.85}Sb_{0.15}$ multiple quantum wells (MQW) as the active region. The RCLED exhibits (85x) higher peak intensity, (13x) higher integrated output power, (16x) narrower spectral linewidth and (7x) superior temperature stability compared to a reference LED without a resonant cavity.

2. RCLED DESIGN

The schematic structure of the MQW resonant cavity is illustrated in Fig. 1(a). It consists of a single wavelength, 1λ-thick, cavity which is sandwiched between two distributed Bragg reflectors (DBRs). The active region contains 4.5 pairs of $Al_{0.12}In_{0.88}As/InAs_{0.85}Sb_{0.15}$ strained-layer QWs, placed at the center of the cavity corresponding to the antinode position of the electric field intensity as shown in Fig. 1(b) in order to obtain maximum enhancement. The energy band diagram of the MQW structure was simulated using *nextnano* and shows the band alignment is type I, as depicted in the inset of Fig. 1(c), where the (e1-hh1) ground state transition occurs in the InAsSb layer. Type I band alignment and compressive strain (~1%) are employed to maximize e-h overlap and reduce non-radiative Auger recombination respectively. The thickness of the $Al_{0.12}In_{0.88}As$ barrier and $InAs_{0.85}$ $Sb_{0.15}$ quantum well layers were approximately 6 nm and 17 nm, accordingly. All the structures for this study were grown by molecular beam epitaxy (- see methods). The first grown layer was an n-type GaSb buffer layer, followed by a 13.5 pairs lattice–matched undoped $AlAs_{0.08}$ $Sb_{0.92}$/GaSb bottom-DBR mirror. On top of the bottom-DBR, a 1λ-thick micro-cavity was grown as follows: an *n*-doped $InAs_{0.90}Sb_{0.10}$ layer; *i*-AlInAs/InAsSb QWs; a 10 nm-thick *p*-doped AlSb barrier layer; and a *p*-doped $InAs_{0.90}Sb_{0.10}$ layer. The AlSb barrier layer provides a strong electron confinement inside the AlInAs/InAsSb MQW region because of the high conduction band offset at the heterointerface of the active region as shown in Fig. 1 (c). After that, the top-DBR mirror comprising 5 pairs of *p*-doped $AlAs_{0.08}Sb_{0.92}$/GaSb was grown to finalize the resonant cavity structure. The total thickness of the completed RCLED structure is around 13 μm.

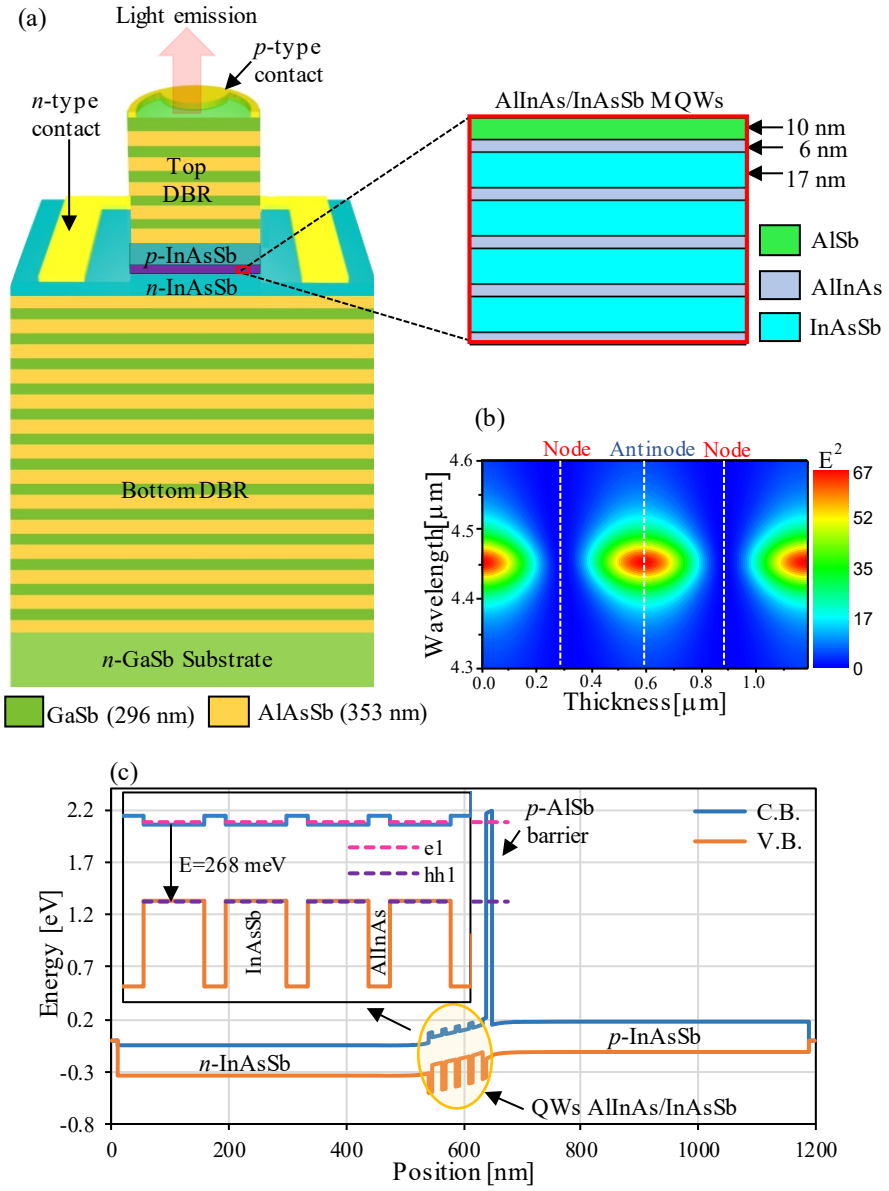

Fig. 1. (a) A schematic diagram of the MQW resonant cavity LED structure showing the details of the AlInAs/InAsSb MQW in the active region of the p-i-n diode within the AlAsSb/GaSb DBRs, which form the microcavity, (b) The calculated electric field intensity distribution inside the cavity showing the position of the antinodes. (c) The energy band diagram of the RCLED active region calculated using *nextnano*, showing the electron-blocking barrier. Details of the type I band alignment in the MQW are highlighted in the inset. See also Supplementary Information Fig.S1.

Numerical modelling was used to evaluate the emission enhancement of the full resonant-cavity structure and the reflectivity of the top and bottom DBR mirrors based on our previous work [35]. The quality factor (Q), the emission rate enhancement at the resonance wavelength (G_e) and the integrated emission enhancement (G_{int}) can be derived as: [36]

$$Q = m\frac{\pi\sqrt[4]{R_1R_2}}{1-\sqrt{R_1R_2}} \quad (1)$$

$$G_e \approx \frac{\xi}{2}\frac{2}{\pi}\frac{\pi(R_1R_2)^{1/4}(1-R_1)}{\left(1-\sqrt{R_1R_2}\right)^2}\frac{\tau_{cav}}{\tau} \quad (2)$$

$$G_{int} \approx G_e\sqrt{\pi \ln 2}\frac{\Delta\lambda_{cav}}{\Delta\lambda_{ref}} \quad (3)$$

where R_1 and R_2 are the reflectivity of the top and bottom DBR mirror, respectively, ξ is the antinode enhancement factor, and $\Delta\lambda_{ref}$ is the linewidth of the active region. The linewidth of the resonant cavity mode $\Delta\lambda_{cav}$ is related to the cavity quality factor Q via the relation: [36]

$$\Delta\lambda_{cav} = \lambda_{cav}/Q \quad (4)$$

where λ_{cav} is the position of the optical mode. The cavity order m is related to the cavity thickness d_{cav} by $m = 2n_{cav}d_{cav}/\lambda_{cav}$, where n_{cav} is the refractive index of the cavity. For low values of m, high extraction efficiency should be achieved owing to the greater overlap between the cavity response and the underlying emission spectrum. [28,37] Therefore, we selected $d_{cav} = \lambda$ corresponding to $m = 2$.

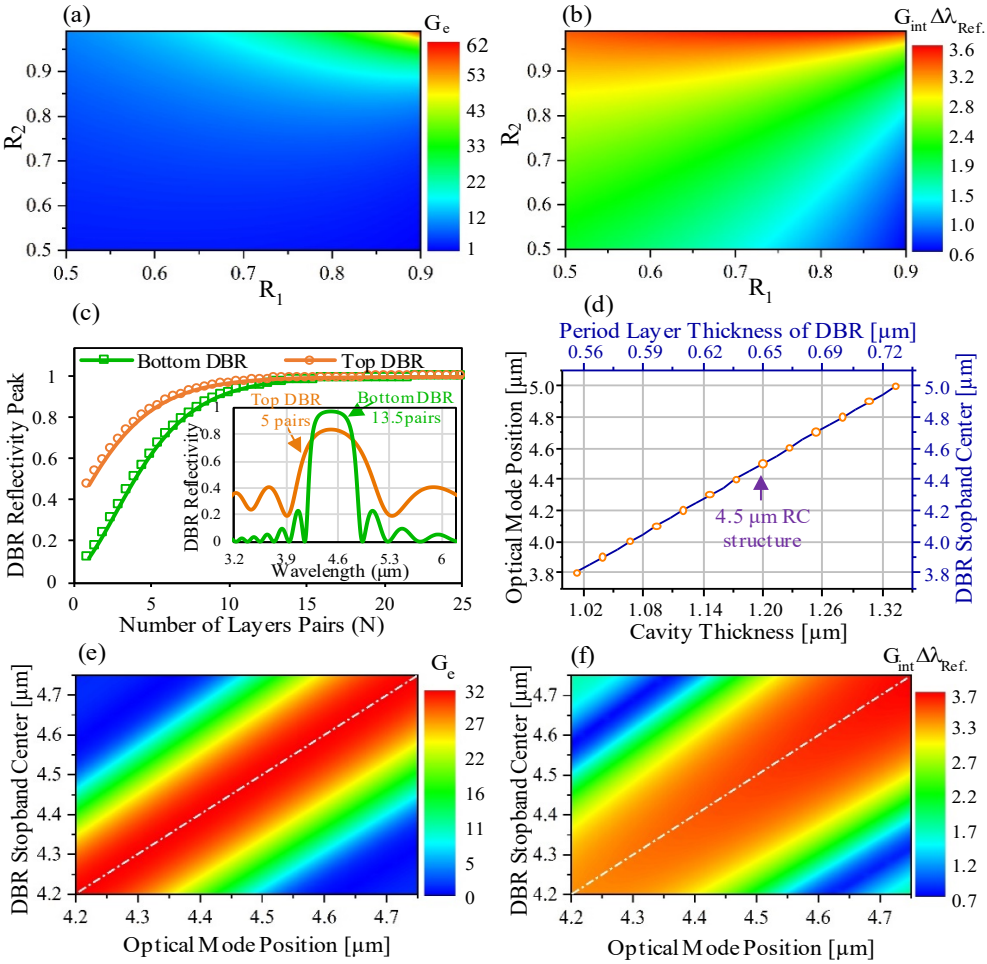

Fig. 2. (a) and (b) Room temperature simulations of the resonant emission (G_e) enhancement factor, and the integrated emission (G_{int}) enhancement factor as a function of the top and bottom DBR mirror reflectivity, R_1 and R_2, respectively. (c) The peak DBR reflectivity as a function of the number of layer pairs (N). The inset shows simulations of the DBR reflectivity vs wavelength for 13.5 pairs (bottom) and 5 pairs (top) DBR. (d) The resonance condition between the optical mode and the DBR stopband center vs the cavity thickness and the DBR period layer thickness, respectively. (e) and (f) Room temperature simulations of the resonance emission (G_e) and the integrated emission (G_{int}) enhancement factor as a function of the DBR stopband center and the peak emission of the cavity mode, respectively. The white dashed-dotted line represents the resonance case between the optical cavity mode and the DBR stopband center.

Figures 2(a) and 2(b) show the emission rate enhancement at the resonance wavelength and the integrated emission enhancement as a function of the DBR mirror reflectivity. The highest integrated emission enhancement (G_{int}) is achieved when $R_2 > 95\%$, and $50\% < R_1 < R_2$. Furthermore, in order to obtain a high emission enhancement factor (G_e) of more than say 30 times, R_2 and R_1 should be greater than 96% and 82%, respectively. The reflectivity of the DBR mirrors was modelled using a transfer matrix method [38], with the refractive indices of $n_L \approx 3.16$ for AlAsSb and $n_H \approx 3.76$ for GaSb. The main advantage of this layer combination is the large refractive index contrast ($\Delta n \sim 0.6$), which requires fabricating only a few quarter-λ-thick layer pairs to achieve high reflectivity. The simulation results indicate that 13.5 periods of the bottom DBR and 5 periods of the top DBR are sufficient to achieve high reflectivity, $R_2 > 97\%$ and $R_1 > 83\%$, as shown in Fig. 2(c). (The half period is necessary for phase matching). The stopband center of the DBR (λ_{DBR}) and the optical mode position of the microcavity (λ_{cav}) are related to the period layer thickness of the DBR mirror ($\mathrm{d_L} + \mathrm{d_H}$) and the cavity thickness ($\mathrm{d_{cav}}$), respectively, via the relations: [36]

$$\lambda_{\mathrm{DBR}} = 2(\,\mathrm{n_L d_L} + \mathrm{n_H d_H}) \quad (5)$$

$$\lambda_{\mathrm{cav}} = \mathrm{n_{cav} d_{cav}} \quad (6)$$

Where, $\mathrm{d_L}$ and $\mathrm{d_H}$ are the thickness of the alternating DBR layers of the AlAsSb and GaSb, respectively and $\mathrm{n_{cav}}$ is a weighted average of the refractive indices. Ideally, (i) the optical mode wavelength (λ_{cav}) and the emission in the active region ($\lambda_{\mathrm{source}}$) should be in resonance, (ii) the MQW in the active region should be located at an antinode of the electric field inside the cavity, (iii) there should be resonance between λ_{DBR} and λ_{cav}. We calculated the values of the λ_{DBR} and λ_{cav} at resonance as a function of the DBR period thickness ($\mathrm{d_L} + \mathrm{d_H}$) and the cavity thickness ($\mathrm{d_{cav}}$), respectively. The results are plotted in Fig. 2(d). A small change in the thickness of $\mathrm{d_{cav}}$ and/or $\mathrm{d_L} + \mathrm{d_H}$ leads to a change in λ_{cav} and λ_{DBR}, respectively, causing detuning between λ_{cav} and λ_{DBR}. From calculation, it was found that when the thickness increases or decreases by 1% (which could occur during MBE growth), then λ_{cav} shifts towards longer/shorter wavelength by 45 nm and λ_{DBR} shifts by 40 nm. The detuning between λ_{cav} and λ_{DBR}, is considered theoretically in Figs. 2(e) and 2(f) which map the effect of detuning on G_{int} and G_e, respectively. The dashed-dotted line represents the resonance case between λ_{cav} and λ_{DBR}, where maximum emission enhancement is achieved. Our results show that even if there is some detuning, G_{int} and G_e still maintain high values over a wide wavelength range, depending on the bandwidth of the DBR stopband. For example, when the detuning between λ_{DBR} and λ_{cav} is about 100 nm, the values of G_{int} and G_e decrease by 3% and 11% respectively.

3. MATERIALS AND METHODS

The MQW RCLED was grown lattice-matched on (001) n-doped GaSb substrate using a Veeco GenXplor molecular beam epitaxy (MBE) reactor with "SUMO" effusion cells for Al, Ga and In, and valved cracker cells for As and Sb fluxes respectively. V/III ratios were maintained at ~1.6:1. Growth temperatures were calibrated using the oxide desorption temperature (540 °C) and a 3x/5x RHEED transition occurring around 425 °C (depending on the V-III ratio). The growth temperatures were 505 °C for AlAsSb and GaSb, 425 °C for the QW layers and 445 °C for the InAsSb cavity layers. All growth rates were < 1 ML/s, with 0.75 ML/s for AlAsSb, 0.95 ML/s for GaSb, 0.25 ML/s for InAsSb and 0.75 ML/s for AlInAs.

Device processing was carried out using standard photolithography and wet chemical etchants followed by Ti/Au metallization for the ohmic contacts. In particular, the InAsSb layers were etched using citric acid: H_2O_2 (2: 1) while sulfonic acid:H_2O_2: H_2O (1:8:80) was used for etching the AlInAs/InAsSb QWs. GaSb and AlAsSb were etched using a dilute ammonia based etchant. The Ti/Au top contact for the *p*-side of the RCLED was deposited on the top *p*-type GaSb DBR layer by thermal evaporation and metal lift-off. A second photolithography step was carried out to pattern the sample for subsequent wet etching of the mesa, by etching through the

structure and stopping within the *n*-InAsSb layer. Finally, a Ti/Au metal contact was deposited on the *n*-InAsSb layer to provide an ohmic contact for the n-side. In the case of the reference LED, (which was essentially the same as the RCLED but without the Bragg mirrors) the Ti/Au top contact for the p-side was deposited on the top p-type InAsSb layer and the bottom contact was deposited on the *n*-InAsSb layer following wet etching. The structure of the RCLED is illustrated in Fig. 1(a). A cross sectional SEM image of the completed RCLED structure is given in the supplementary material.

After fabrication, the optical transmission and the electroluminescence measurements of the samples were obtained using a Bruker Vertex 70 Fourier transform infrared (FTIR) spectrometer, with a spectral resolution of 0.5 cm^{-1}. The system is associated with a temperature-controlled Oxford Instruments continuous flow liquid-helium cryostat to record temperature dependence of the electroluminescence spectra. The electroluminescence emission spectra of the RCLED were systematically measured over the temperature range from 20 K to 300 K and compared with a reference LED without any DBR mirrors. To avoid Joule heating at high currents, the RCLED was tested using a short (1%) duty cycle so that we were able to reliably record the peak spectral intensity. To record the emission spectra our detection system requires a larger duty cycle (30%) for which a lower drive current was used. The energy band diagram of the cavity layers of the RCLED structure was modelled using *Nextnano*.

4. RESULTS

4.1 Microcavity enhancement of mid-infrared electroluminescence

The transmission spectrum of the MQW resonant-cavity structure and the electroluminescence spectrum of the MQW RCLED measured using a Fourier-transform infrared (FTIR) spectrometer at room temperature are shown in Fig. 3(a). The wavelength of the main emission peak occurs at 4.462 µm, corresponding to the wavelength of the resonant cavity mode in the transmission spectrum. (The small emission peaks on either side of the main peak originate from fluctuations in cavity transmission). Fig. 3(b) compares the electroluminescence emission spectra of the RCLED and reference LED measured at 300 K using the same quasi-continuous injection current of 100 mA at 1 kHz with 30% duty cycle.

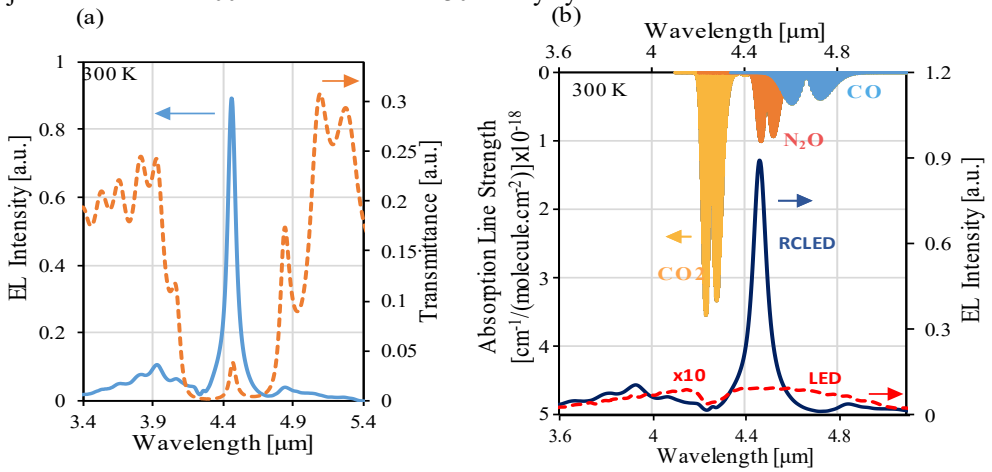

Fig. 3. (a) Experimentally measured transmission spectrum (dashed line) and electroluminescence emission spectrum (solid line) of the RCLED structure at 300 K, showing that the wavelength of the main emission peak occurs at 4.462 µm, which corresponds closely to the cavity resonance wavelength of 4.446 µm. (b) Comparison of the RCLED (solid line) and the reference LED (dashed line) electroluminescence emission spectra at 300 K using the same injection current (100 mA at 1 kHz with 30% duty cycle). The dip in the reference LED spectrum originates from atmospheric CO_2 absorption in the optical path. Also shown are the fundamental fingerprint absorptions of greenhouse gases of interest in this spectral range.

As shown in Fig. 3(b), at room temperature the 800 µm-diameter-RCLED peak emission at 4.462 µm overlaps nicely with the fundamental N_2O fingerprint absorption. The linewidth at full width at half maximum (FWHM) of the RCLED is 70 nm, which is 16x narrower than the MQW reference LED, so that substantially more *useable* photons fall within the N_2O absorption envelope. With minor adjustments to the microcavity dimensions, the peak position and spectral overlap can be optimised, or adjusted to detect CO_2 or CO, without changing the Sb content in the MQW (– see discussion). In addition to reducing the linewidth, the resonant cavity enhancement has the effect of significantly increasing the peak emission intensity by 85x, with an increase in the total integrated emission (average output power) of 13x, which corresponds to an emittance of 2.5 $mWcm^{-2}$ and a spectral intensity of 36 $\mu Wcm^{-2}nm^{-1}$ under quasi-cw conditions. By comparison, the 400 µm-diameter RCLED exhibits an emittance of ~10 $mWcm^{-2}$ and a spectral intensity of ~140 $\mu Wcm^{-2}nm^{-1}$. Under pulsed operation the spectral intensity compares favourably with that of commercial devices [39] and non-resonant structures [40,41]. Conventional, non-resonant LEDs can be series connected in a small array to increase output power for gas sensing but much of this radiation lies outside the gas absorption band [42,43]. As mentioned earlier, interband cascade LEDs (ICLEDs) at shorter wavelengths exhibit higher cw output power at 300 K [17,38], spread over a larger linewidth (FWHM ~ 500-1000 nm). At longer wavelengths thermal management is more critical and high injection necessitates operation at short duty cycles [21,23]. Figure 4 shows the peak spectral intensity of our RCLED measured using a 1% duty cycle to minimise Joule heating; as our device does not yet have the benefit of optimised ohmic contacts, epi-side down mounting, or a heat spreader. Recent results from a 16-stage 4.5 µm ICLED at 0.1% duty cycle (Muhowski et al. [23]) together with a 5-stage ICLED at 1% duty cycle, made in our laboratory [21] are also shown in Fig. 4 for comparison, where the spectral intensity of the RCLED performs favourably well, reaching > 2 $mWcm^{-2}nm^{-1}$ for the 400 µm-diameter-RCLED. The spectral intensity of the 800 µm-diameter-RCLED is lower due to higher current density in the 400 µm-diameter-RCLED.

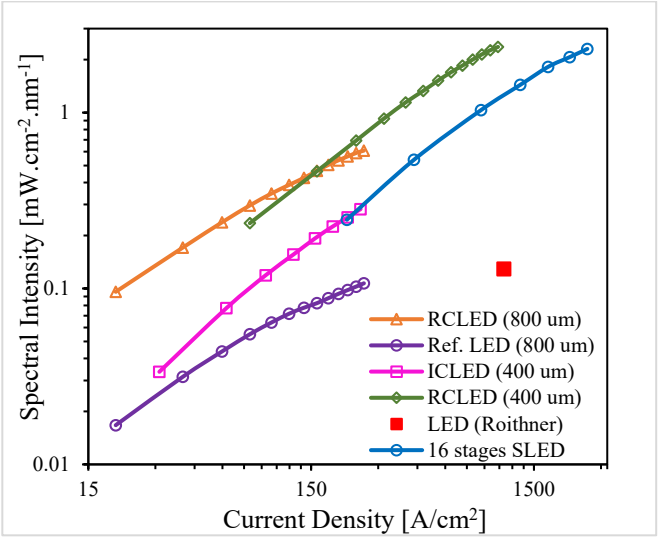

Fig. 4. The spectral intensity of two RCLEDs of different diameter vs current density, measured at room temperature using a 1 kHz injection current with 1% duty cycle. The MQW reference LED is also shown (x30) together with other results from the literature measured under similar conditions, including a 16-stage 4.5 µm ICLED at 0.1% duty cycle (adapted from Muhowski et al.[23]) and an ICLED at 1% duty cycle made in our laboratory (400 µm x 400 µm) [21]. The conventional 4.6 µm LED spectral intensity was estimated from the peak power given in the data sheet [39].

All the devices exhibit some rollover at high injection, due to the build-up of non-radiative Auger recombination. The 400 µm dia. RCLED exhibits more linear performance, which we attribute to increased ohmic loss due to the higher current drawn in larger area devices. This is also evident in the ICLEDs.

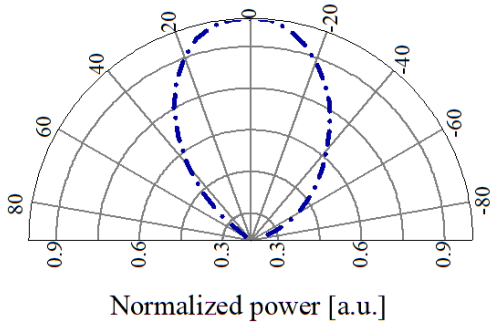

Fig. 5. Far field angular profile of the RCLED emission, which shows a half power solid angle of 45°.

The far-field technique was used to measure the angular emission profile of the RCLED, where the distance between the emitter and the detector was 1 cm. Using this method, the emission intensity was measured from the top surface and the vertical facets. At room temperature, the results exhibited a single-lobe emission profile with a half power solid angle of 45° as illustrated in Fig. 5, showing a better directionality compared with that of our previous work [35].

4.2 Temperature dependence of the emission

The electroluminescence emission spectra of the RCLED and reference LED measured at different temperatures in the range 20 K - 300 K, using 100 mA injection current at 30% duty cycle and 1 kHz, are shown in Figs. 6(a) and 6(b), respectively. Over this temperature range the intensity of the RCLED decreased by only a factor of 4 whereas the reference LED decreased by a factor of ~500. As shown in Fig. 6(c), over the temperature range from 20 K to 200 K, the RCLED peak emission intensity remains approximately constant. Then above 200 K the intensity decreases more gradually. Consequently, the relative intensity increases with temperature until T≈240 K and then slightly decreases. This is consistent with spectral detuning between the emission of the AlInAs/InAsSb MQWs in the active region and the cavity mode. In addition, the electroluminescence emission peak of the RCLED red shifts to longer wavelengths with increasing temperature but much more slowly compared to the reference LED. This behaviour arises because in the reference LED the wavelength shift of the electroluminescence spectrum is due to the narrowing of the active region bandgap with temperature. However, for the RCLED, the electroluminescence peak position also depends on the microcavity resonant optical mode, which is determined by the thickness and the refractive index of the materials forming the cavity. Based on our previous work [35], the thickness variation of the cavity was calculated as a function of temperature and accounts for less than 4% of the total wavelength shift, so that the main contribution originates from the temperature variation of the refractive index [44,45]. Consequently, the main electroluminescence emission peak of the RCLED shifts by only ~102 nm at a rate of 0.36 nm/K, while the peak of the reference LED shifts by ~600 nm at a rate of ~2.45 nm/K. This represents a factor of 7 improvement in the emission wavelength stability with temperature, which is particularly useful in applications such as gas detection where wavelength stability is required to ensure the emission peak remains within the gas absorption envelope as the sensor temperature varies.

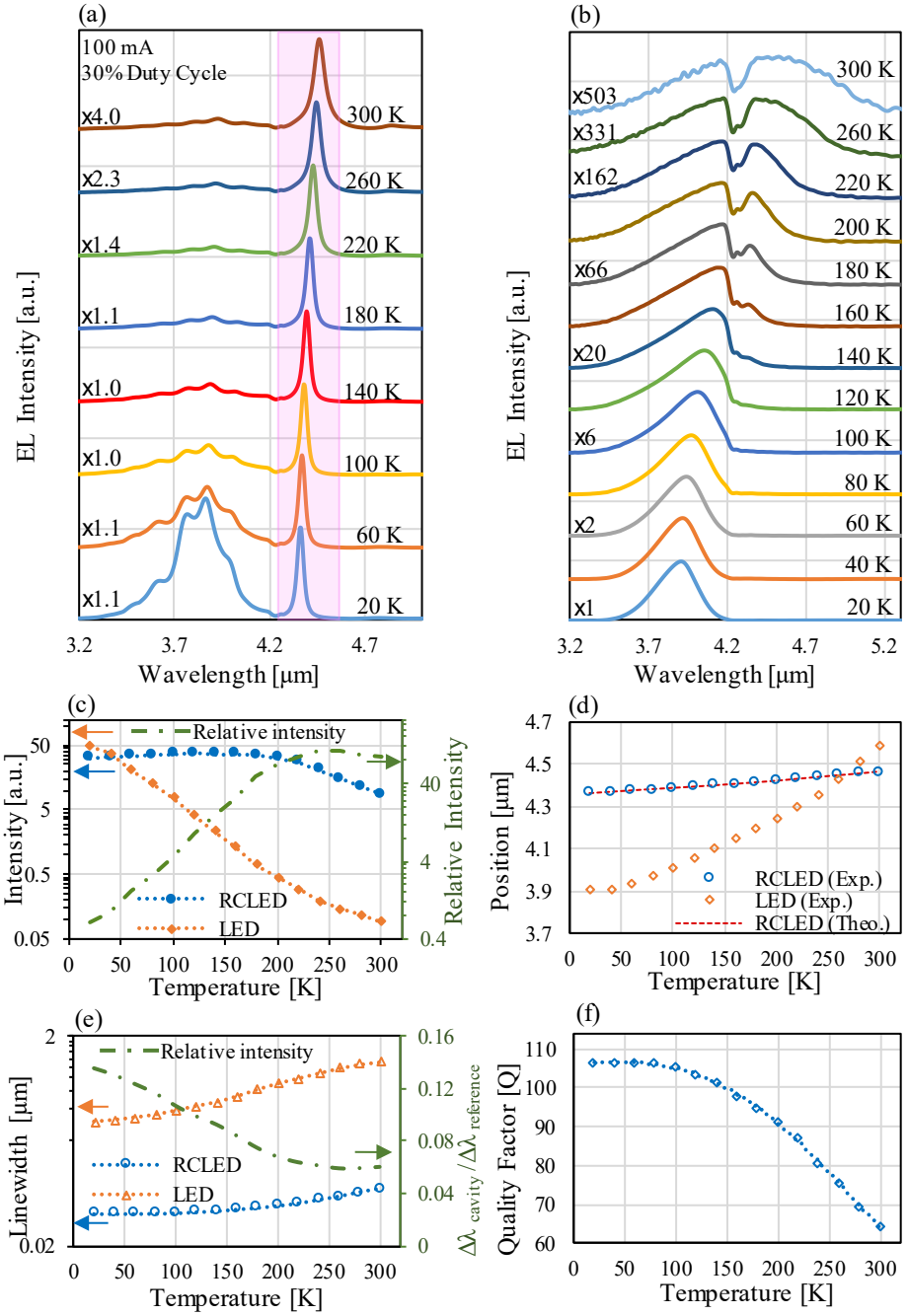

Fig. 6. Temperature dependence of the electroluminescence emission for (a) the RCLED and (b) the reference LED without DBR, both measured using 100 mA, 30% duty cycle at 1 kHz. The shaded area in (a) represents the DBR stop band (c) Peak intensity values of the electroluminescence from the RCLED and reference LED. The dashed-dotted line represents the relative intensity. (d) The red shift in wavelength of the electroluminescence peaks as a function of temperature. The dashed line represents the theoretical values for the RCLED peak wavelength. (e) Linewidth of the electroluminescence spectra of the RCLED and reference LED as a function of temperature. The dashed-dotted line represents the relative linewidth ($\Delta\lambda_{cavity}/\Delta\lambda_{reference}$). (f) Quality factor of the RCLED as a function of temperature.

Good agreement between the experimentally observed spectral shift and the theoretically calculated dependence was achieved as shown in Fig. 6(d) based on the relation given in equations (6) - (9). The parameters, λ_{cav}, n_{cav}, and d_{cav} are functions of temperature. The temperature-dependent refractive index of the cavity ($n_{cav}(T)$) was determined by interpolation for the alloy constituents using the temperature coefficient of the refractive index for $Al_xIn_{1-x}As$ [46-48]

$$\frac{1}{n}\left(\frac{dn}{dT}\right) = [1.2 \times 10^{-4}x + 4.6 \times 10^{-5}(1-x)]K^{-1} \quad (7)$$

and similarly for $InAs_xSb_{1-x}$ given by, [47,49]

$$\frac{1}{n}\left(\frac{dn}{dT}\right) = [1.2 \times 10^{-4}x + 6.90 \times 10^{-5}(1-x)]K^{-1} \quad (8)$$

where the temperature dependence of the refractive index of the InAs is calculated from [49],

$$2n\left(\frac{dn}{dT}\right) = 2.18 \times 10^{-3}K^{-1} \quad (9)$$

From Fig. 6(e), over the temperature range from 20 K to 100 K, it was found that there is no noticeable change in the RCLED linewidth, which is measured to be 41 nm. As the temperature increases above 100 K, the FWHM increases to 70 nm at 300 K. However, the linewidth of the reference LED rapidly becomes broader (FWHM ~300 nm at 20 K and ~1140 nm at 300 K), since it is determined by the joint density of states in the bands and the thermal energy of carriers [24]. In contrast, the RCLED linewidth depends on the quality factor (Q) of the resonant cavity, which is shown in Fig. 6(f) –obtained by inverting equation (4). It can be seen that the quality factor decreases with increasing temperature, as the reflectivity of the DBR mirrors decreases as the temperature increases. Furthermore, the RCLED can be tailored to match the absorption spectrum of the target gas by adjusting the cavity and DBR properties.

In order to evaluate the intensity enhancement factor, the ratio of the peak electroluminescence intensity of the RCLED to that of the reference LED is shown in Fig. 7(a) over the range 140 K-300 K. The power (integrated) enhancement factor (G_{int}), defined as the output power ratio of the RCLED to the reference LED, is related to the intensity enhancement factor (G_e) by the relation: [36]

$$G_{int} = G_e\sqrt{\pi ln2}\,\frac{\Delta\lambda_{cavity}}{\Delta\lambda_{reference}} \quad (9)$$

The intensity enhancement factor of the RCLED decreases with increasing temperature due to the decrease in the cavity Q-factor. Figure 7(b) shows that both the output power of the RCLED and reference LED decrease as a function of temperature. As mentioned earlier, when T<260 K, the quantity $\Delta\lambda_{cavity}/\Delta\lambda_{reference}$ and the intensity enhancement factor decrease as temperature increases. Consequently, the integrated enhancement factor should also decrease as the temperature increases. However, because the cavity resonance implicit in equation (9) is not satisfied at all temperatures (Fig. 7(c)), the integrated enhancement increases with temperature, as shown in Fig. 7(b). The emission spectrum of the RCLED shifts to longer wavelengths more slowly compared to that of the reference LED –see Figs. 7(d) – (g). Consequently, the difference between the peak wavelengths (spectral detuning) decreases gradually with increasing temperature and becomes zero at around T=260 K, as shown in Fig. 7(c). Therefore, the power enhancement in Fig. 7(b) levels off above 260 K due to broadening of the QWs emission. Our results also show a greater intensity enhancement factor compared to previous work [28,34,35].

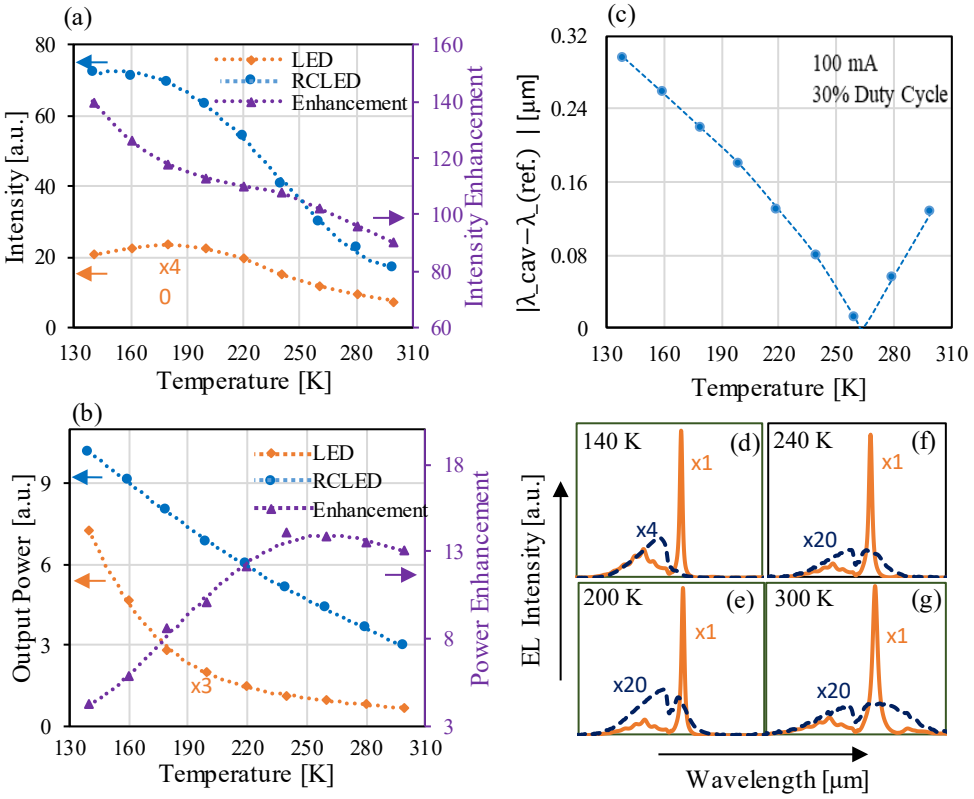

Fig. 7. (a) Temperature dependence of the peak emission intensity of the RCLED and the reference LED, both measured using 100 mA, 30% duty cycle at 1 kHz. (b) Temperature dependence of the output power for the RCLED and reference LED. (c) The temperature dependence of the spectral detuning of the cavity mode and the reference peak emission. The dashed lines are a guide to the eye. (d)-(g) Electroluminescence spectra of the RCLED (solid) and reference LED (dashed) at different temperatures, 140 K, 200 K, 240 and 300 K respectively, using the same drive conditions.

5. DISCUSSION

Resonant cavity enhancements are due to constructive interference of light in the cavity, which increases the amount of light emitted towards the surface within the escape angle from the high-index semiconductor material into air. The cavity enhances the propagation of optical modes, which match the optical length of the cavity, whereas the other modes are suppressed [45] (i.e. the optical mode density is strongly enhanced for on-resonance wavelengths). We also note that the associated decrease in spontaneous lifetime makes non-radiative Shockley-Read processes less important. The main difference compared to a VCSEL is the criterion that $(1-R_{out})>>\alpha d_{active}$, where d_{active} is the thickness and α is the absorption coefficient of the active region and R_{out} is the reflectivity of the out-coupling mirror. This ensures that more light escapes the cavity than gets re-absorbed in the active region because the device emits only spontaneous emission. By carefully combining InAsSb strained MQW with high contrast AlAsSb/GaSb DBR mirrors our design enables an RCLED with high spectral brightness within a narrow linewidth which is well suited to selective gas detection and optical spectroscopy. The emission wavelength is determined by the Sb content in the MQW but also by the construction of the resonant cavity. The emission enhancement, linewidth and Q-factor are strongly dependent on the DBR mirror reflectivity. The high refractive index contrast ($\Delta n = 0.6$) between AlAsSb and GaSb means that relatively few pairs of layers are needed to achieve sufficiently high reflectivity.

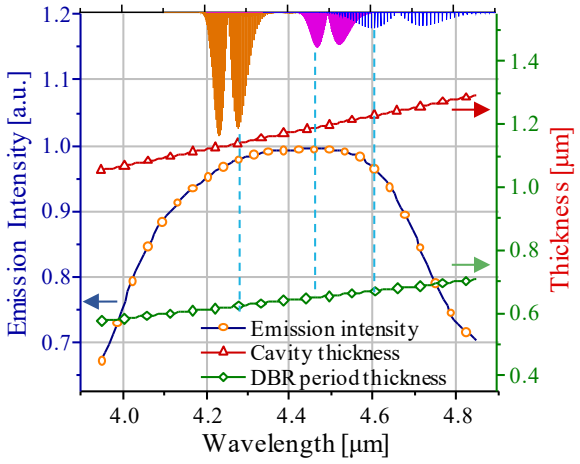

Fig. 8. The calculated variation in RCLED wavelength and emission intensity dependence on cavity thickness or DBR period thickness. Also shown are the absorption spectra of key greenhouse gases to illustrate the accessible tuning range, which encompasses CO_2, N_2O and CO.

Figure 8 shows the accessible spectral range for our RCLED extends from 3.9 μm to 4.9 μm – maintaining 70% of the peak emission intensity. We estimated the effect on the emission intensity keeping the same MQWs in the active region and changing the thickness of the cavity (red line) and the DBR layers (green line). The results show that if the thickness of the DBR layers and the cavity are both reduced by 4.5%, then the emission peak readily tunes down in wavelength to 4.25 μm, which is well matched to CO_2 detection. Meanwhile, the emission intensity is decreased by only 3% from that of our MQW RCLED at 4.5 μm. Similarly, for CO detection at 4.6 um, the thickness of the DBR layers and the cavity simply needs to be increased by 3%, where the emission intensity is again reduced only slightly by 3%. This is possible because of the relatively broadband emission of the AlInAs/InAsSb MQWs in the active region. Consequently, our RCLED design is readily able to address three important greenhouse gases.

The emission wavelength of the RCLED can be tuned further out to longer wavelengths by adjusting the Sb content in the MQW – although this requires a corresponding redesign of the DBRs and cavity (- see also supplementary information). However, due to lattice mismatch and strain considerations, with 15% Sb the QW are type I with a conduction band offset of 30 meV. This means that the emission wavelength cannot be significantly increased without the structure becoming type II, resulting in a likely reduction in output power. On the other hand reducing the Sb content would provide larger conduction band offset with deeper confinement and enable RCLED emission down to ~4.0 μm. However, tensile strain limitations on the critical thickness prevents the realization of RCLEDs at shorter wavelengths. Increasing the number of periods in the upper/lower DBR would have the effect of increasing the cavity finesse and Q-factor which would result in a narrower spectral linewidth and higher optical output at the resonance wavelength but lower overall output power. However, output power could be increased by using a number of RCLED chips in a small array - as implemented by GSS Ltd. in their COZIR sensor [42] which employs 9 LED elements. The resonant cavity concept can also be applied to enhance detector performance and recently we demonstrated a resonant cavity detector operating at around 4.41 μm with peak responsivity of 3.0 AW^{-1}, corresponding to quantum efficiency of 84%. [50] Clearly, it is also possible to implement a resonant cavity LED - resonant detector pair to obtain even higher sensitivity although care is needed to maintain effective matching of the resonance peaks.

6. CONCLUSION

In conclusion, we have demonstrated a novel mid-infrared resonant cavity LED operating near 4.5 μm at room temperature, which is well matched to the N_2O gas absorption. The RCLED exhibits (85x) higher peak intensity, (13x) higher integrated output power, (16x) narrower spectral linewidth and (7x) superior temperature stability compared to a reference LED without a resonant cavity. Our RCLED structure design uses a 1λ-thick microcavity formed from high refractive index contrast AlAsSb/GaSb DBR mirrors to enhance light extraction from the AlInAs/InAsSb QWs located at the central antinode, while an AlSb blocking barrier prevents electrons escaping from the active region. Because the emission wavelength of the cavity mode is determined mainly by the temperature coefficient of the refractive index of the cavity materials, the emission peak of the RCLED shifts toward longer wavelengths as temperature increases at a rate of only 0.362 nm/K. Our results are in excellent agreement with numerical modelling based on an optimized RCLED structure containing 4 $Al_{0.12}In_{0.88}As/InAs_{0.85}Sb_{0.15}$ QWs in the active region, with 13.5 lattice–matched $AlAs_{0.08}Sb_{0.92}$/GaSb ($\lambda/4$) pairs for the bottom DBR and 5 pairs for the top DBR of the microcavity. Owing to the increased brightness, narrower linewidth and improved temperature dependence, our results show that this RCLED design forms an excellent basis for the further development of compact sources for gas sensor instruments as well as spectroscopy. The RCLED is superior to conventional mid-infrared LEDs, having higher spectral intensity and providing significantly more *useable* photons at the required target wavelength. Meanwhile, it is less complex and more cost-effective than a quantum cascade laser and so leads the way for practical implementation in applications such as local N_2O detection in silage making, car exhaust emissions monitoring etc. Furthermore, carefully adjusting the cavity dimensions enables the emission wavelength to be readily tailored over a wider spectral range to target other greenhouse gases.

Acknowledgments

F. A. Al-Saymari was supported by a studentship funded by the ministry of higher education in Iraq. We gratefully acknowledge funding from EPSRC (grant EP/M013707/1), and also from the Royal Academy of Engineering for providing a Research Fellowship (10216/114) awarded to P.J. Carrington.

Disclosures

The authors declare no conflicts of interest.

See Supplement Fig. S1 for supporting content

REFERENCES

1. B. Matveev, N. Zotova, S. Karandashov, M. Remennyi, N. IL'Inskaya, N. Stus, V. Shustov, G. Talalakin, J. Malinen, "InAsSbP/InAs LEDs for the 3.3-5.5 mu m spectral range," *IEE Proceedings-Optoelectronics* **145**, 254-256 (1998).

2. A. Krier, H. H. Gao, V. V. Sherstnev, Y. Yakovlev, "High power 4.6 μm light emitting diodes for CO detection," *J. of Phys. D: Appl. Phys.* **32**, 3117-3121 (1999).

3. H. H. Gao, A. Krier, V. Sherstnev, Y. Yakovlev, "InAsSb/InAsSbP light emitting diodes for the detection of CO and CO_2 at room temperature," *J. of Phys. D: Appl. Phys.* **32**, 1768-1772 (1999).

4. M. J. Pullin, H. R. Hardaway, J. D. Heber, C. C. Phillips, W. T. Yuen, Ra A. Stradling, P. Moeck, "Room-temperature InAsSb strained-layer superlattice light-emitting diodes at λ=4.2 μm with AlSb barriers for improved carrier confinement," *Appl. Phys. Lett.* **74**, 2384-2386 (1999).

5. A. Krier, V. V. Sherstnev, "Powerful interface light emitting diodes for methane gas detection," *J. of Phys. D: Appl. Phys.* **33**, 101-106 (2000).

6. P. J. Carrington, Q. Zhuang, M. Yin, A. Krier, "Temperature dependence of mid-infrared electroluminescence in type II InAsSb/InAs multiquantum well light-emitting diodes," *Semi. Sci. and Tech.* **24**, 075001 (2009).

7. T. D. Mishima, J. C. Keay, N. Goel, M. A. Ball, S. J. Chung, M. B. Johnson, M. B. Santos, "Effect of structural defects on InSb/$Al_xIn_{1-x}Sb$ quantum wells grown on GaAs (001) substrates," *Physica E-Low-Dimensional Systems & Nanostructures* **20**, 260-263 (2004).

8. T. Ashley, C. T. Elliott, N. T. Gordon, R. S. Hall, A. D. Johnson, G. J. Pryce, "Uncooled InSb/$In_{1-x}Al_xSb$ mid infrared emitter," *Applied Physics Letters* **64**, 2433-2435 (1994).

9. B. Mirza, G. Nash, S. Smith, M. Haigh, L. Buckle, M. Emeny, T. Ashley, "InSb/$Al_xIn_{1-x}Sb$ quantum-well light-emitting diodes with high internal quantum efficiencies," *Applied Physics Letters* **89**, (2006).

10 H. Fujita, K. Ueno, O. Morohara, E. Camargo, H. Geka, Y. Shibata, N. Kuze, "AlInSb Mid-Infrared LEDs of High Luminous Efficiency for Gas Sensors," *Physica Status Solidi a-Applications and Materials Science* **215**, (2018).

11. L. Meriggi, M. J. Steer, Y. Ding, I. G. Thayne, C. MacGregor, Ch. N. Ironside, M. Sorel, "Enhanced emission from mid-infrared AlInSb light-emitting diodes with p-type contact grid geometry," *Journal of Applied Physics* **117**, (2015).

12. M. Aziz, Ch. Xie, V. Pusino, A. Khalid, M. Steer, I.G. Thayne, D. RS. Cumming, "Multispectral mid-infrared light emitting diodes on a GaAs substrate," *Appl. Phys. Lett*. **111**, 102102 (2017).

13. M. Nedeljkovic, J. S. Penades, V. Mittal, G. S. Murugan, A. Z. Khokhar, C. Littlejohns, L. G. Carpenter, C. B. E. Gawith, J. S. Wilkinson, G. Z. Mashanovich, "Germanium-on-Silicon Waveguides Operating at Mid-Infrared Wavelengths up to 8.5 μm," *Opt. Express* **25**, 27431−27441 (2017).

14. K. M. Yoo, J. Midkiff, A. Rostamian, Ch. Chung, H. Dalir, R. T. Chen, "InGaAs Membrane Waveguide: A Promising Platform for Monolithic Integrated Mid-Infrared Optical Gas Sensor," *ACS Sensors* **5**, 861-869 (2020).

15. A. Osman, M. Nedeljkovic, J. S. Penades, Y. Wu, Z. Qu, A. Z. Khokhar, K. Debnath, G. Z. Mashanovich, "Suspended Low Loss Germanium Waveguides for The Longwave Infrared," *Opt. Lett.* **43**, 5997−6000 (2018).

16. Y. Zou, S. Chakravarty, Ch. Chung, X. Xu, R. T. Chen, "Mid-infrared silicon2018-MIRReview.pdf photonic waveguides and devices [Invited]," *Photon. Res.* **6**, 254-276 (2018).

17. D. Gibson, C. MacGregor, "A Novel Solid State Non-Dispersive Infrared CO_2 Gas Sensor Compatible with Wireless and Portable Deployment," *Sensors* **13**, 7079-7103 (2013).

18. C. S. Kim, W. W. Bewley, C. D. Merritt, C. L. Canedy, M. V. Warren, I. Vurgaftman, J. R. Meyer, M. Kim, "Improved mid-infrared interband cascade light-emitting devices," *Optical Engineering* **57**, (2018).

19. N. Schäfer, J. Scheuermann, R. Weih, J. Koeth, S. Höfling, "High efficiency mid-infrared interband cascade LEDs grown on low absorbing substrates emitting >5 mW of output power," *Opt. Engr.* **58**, 117106 (2019).

20. C. D. Merritt, C. S. Kim, M. Kim, C. L. Canedy, W. W. Bewley, M. V. Warren, I. Vurgaftman, J. R. Meyer," Effects of ion bombardment on interband cascade laser structures," Proc. SPIE 11288, Quantum Sensing and Nano Electronics and Photonics **XVII**,, 112881N (2020).

21. Y. Zhou, Qi Lu, X. Chai, Z. Xu, A. Krier, L. He, "InAs/GaSb superlattice interband cascade light emitting diodes with high output power and high wall-plug efficiency," *App. Phys. Lett.* **114**, 253507 (2019).

22. R. J. Ricker, S. R. Provence, D. T. Norton, T. F. Boggess, J. P. Prineas, "Broadband mid-infrared superlattice light-emitting diodes," *J. Appl. Phys.* **121**, 185701 (2017).

23. A. J. Muhowski, R. J. Ricker, T. F. Boggess, J. P. Prineas, "n-type anode layer, high-power MWIR superlattice LED," *Appl. Phys. Lett.* **111**, 243509 (2017).

24. E. F. Schubert, Y-H. Wang, A. Y. Cho, L-W. Tu, G. J. Zydzik, "Resonant cavity light-emitting diode," *Appl. Phys. Lett.* **60**, 921-923 (1992).

25. N. E. J. Hunt, E. F. Schubert, R. A. Logan, G. J. Zydzik, "Enhanced spectral power density and reduced linewidth at 1.3 μm in an InGaAsP quantum well resonant-cavity light-emitting diode," *Appl. Phys. Lett.* **61**, 2287-2289 (1992).

26. H. de Neve, J. Blondelle, P. van Daele, P. Demeester, R. Baets, G. Borghs, "Recycling of guided mode light emission in planar microcavity light emitting diodes," *Appl. Phys. Lett.* **70**, 799 (1997).

27. Hadji, E.; Bleuse, J.; Magnea, N.; Pautrat, J. L. "3.2 μm infrared resonant cavity light emitting diode," *Appl. Phys. Lett.* **67**, 2591-2593 (1998).

28. A. M. Green, D. G. Gevaux, Ch. Roberts, Ch. C. Phillips, "Resonant-cavity-enhanced photodetectors and LEDs in the mid-infrared," *Physica E: Low-dimensional Systems and Nanostructures* **20**, 531-535 (2004).

29. A. Ducanchez, L. Cerutti, A. Gassenq, P. Grech, F. Genty, "Fabrication and Characterization of GaSb-Based Monolithic Resonant-Cavity Light-Emitting Diodes Emitting Around 2.3 μm and Including a Tunnel Junction," *IEEE J. of Sel. Top. in Quant. Electro.* **14**, 1014-1021 (2008).

30. Ch. Grasse, P. Wiecha, T. Gruendl, S. Sprengel, R. Meyer, M-C. Amann, "InP-based 2.8–3.5 μm resonant-cavity light emitting diodes based on type-II transitions in GaInAs/GaAsSb heterostructures," *Appl. Phys. Lett.* **101**, 221107 (2012).

31. A. Bachmann, Sh. Arafin, K. Kashani-Shirazi, "Single-mode electrically pumped GaSb-based VCSELs emitting continuous-wave at 2.4 and 2.6 μm," *New J. of Phys*. **11**, 125014 (2009**)**.

32. A. Andrejew, S. Sprengel, M-C. Amann, "GaSb-based vertical-cavity surface-emitting lasers with an emission wavelength at 3 μm," *Opt. Lett.* **41**, 2799-2802 (2016).

33. G. K. Veerabathran, S. Sprengel, A. Andrejew, M-C. Amann, "Room-temperature vertical-cavity surface-emitting lasers at 4 μm with GaSb-based type-II quantum wells," *Appl. Phys. Lett.* **110**, 071104 (2017).

34. L. Meriggi, M. J. Steer, Y. Ding, I. G. Thayne, C. MacGregor, Ch. N. Ironside, M. Sorel, "Development of mid-infrared light-emitting diodes for low-power optical gas sensors," *IEE 11th Conference on Ph.D. Research in Microelectronics and Electronics (PRIME)*, 180-183 (2015).

35. F. A. Al-Saymari, A. P. Craig, Y. J. Noori, Q. Lu, A. R. J. Marshall, A. Krier, "Electroluminescence enhancement in mid-infrared InAsSb resonant cavity light emitting diodes for CO2 detection," *Appl. Phys. Lett.* **114**, 171103 (2019).

36. Schubert, E. F. *Light Emitting Diodes*, Cambridge Press **2006**.

37. H. Benisty, H. De Neve, C. Weisbuch, "Impact of Planar Microcavity Effects on Light Extraction—Part I: Basic Concepts and Analytical Trends," *IEEE J. of Quant. Electron.* **34**, 1612-1631 (1998).

38. M. Born, E. Wolf, *Principle of optics*, Cambridge University Press (1999).

39. http://www.roithner-laser.com/datasheets/led_midir/led46-pr.pdf

40. E. Delli, P. D. Hodgson, E. Repiso, A. P. Craig, P. J. Hayton, Q. Lu, A. R. J. Marshall, A. Krier, P.J. Carrington, "Heteroepitaxial Integration of Mid-Infrared InAsSb Light Emitting Diodes on Silicon," *IEEE Photonics Journal* **11**, 2200608 (2019).

41. M. K. Haigh, G. R. Nash, S. J. Smith, L. Buckle, M. T. Emeny, T. Ashley, "Mid-infrared $Al_xIn_{1-x}Sb$ light-emitting diodes," *Appl. Phys. Lett.* **90**, 231116 (2007).

42. D. Gibson, C. A MacGregor, “Novel Solid State Non-Dispersive Infrared CO_2 Gas Sensor Compatible with Wireless and Portable Deployment,” *Sensors* **13**, 7079-7103 (2013).

43 H. R. Hardaway, T. Ashley, L. Buckle, M. T. Emeny, G. Masterton, G. Pryce, *SPIE Proceedings: Infrared Detector Materials and Devices*, 5564 (2004).

44. W. W. Bewley, C. L. Canedy, C. S. Kim, C. D. Merritt, M. V. Warren, I. Vurgaftman, J. R. Meyer, M. Kim, “Room-temperature mid-infrared interband cascade vertical-cavity surface-emitting lasers,” *Appl. Phys. Lett.* **109**, 151108 (2016).

45. A. B. Ikyo, I. P. Marko, K. Hild, A. R. Adams, S. Arafin, M-C. Amann, S. J. Sweeney, “Temperature stable mid-infrared GaInAsSb/GaSb Vertical Cavity Surface Emitting Lasers (VCSELs)*,*” *Sci. Rep.* 6, 19595 (2016).

46. H. G. Grimmeiss, B. Monemar, “Temperature dependence of the refractive index of AIAs and AIP,” Physica status solidi (a) **5**, 109-114 (1971).

47. J. Talghader, J. S. Smith, “Thermal dependence of the refractive index of GaAs and AlAs measured using semiconductor multilayer optical cavities,” Appl. Phys. Lett. **66**, 335-337 (1995).

48. Adachi. Sadao, *Properties of Group-IV, III-V and II-VI Semiconductors*, England: John Wiley & Sons Ltd (2005).

49. G. D. Gillen, C. DiRocco, P. Powers, Sh. Guha, “Temperature-dependent refractive index measurements of wafer-shaped InAs and InSb,” Applied Optics 47,

50. V. Letka, A. Bainbridge, A. P. Craig, F. Al-Saymari, A. R. J. Marshall, “Resonant cavity-enhanced photodetector incorporating a type-II superlattice to extend MWIR sensitivity,” Optics Express **27**, 23970 (2019).